iScience

CellPress
OPEN ACCESS

Article

Human and mouse PD-L1: similar molecular structure, but different druggability profiles

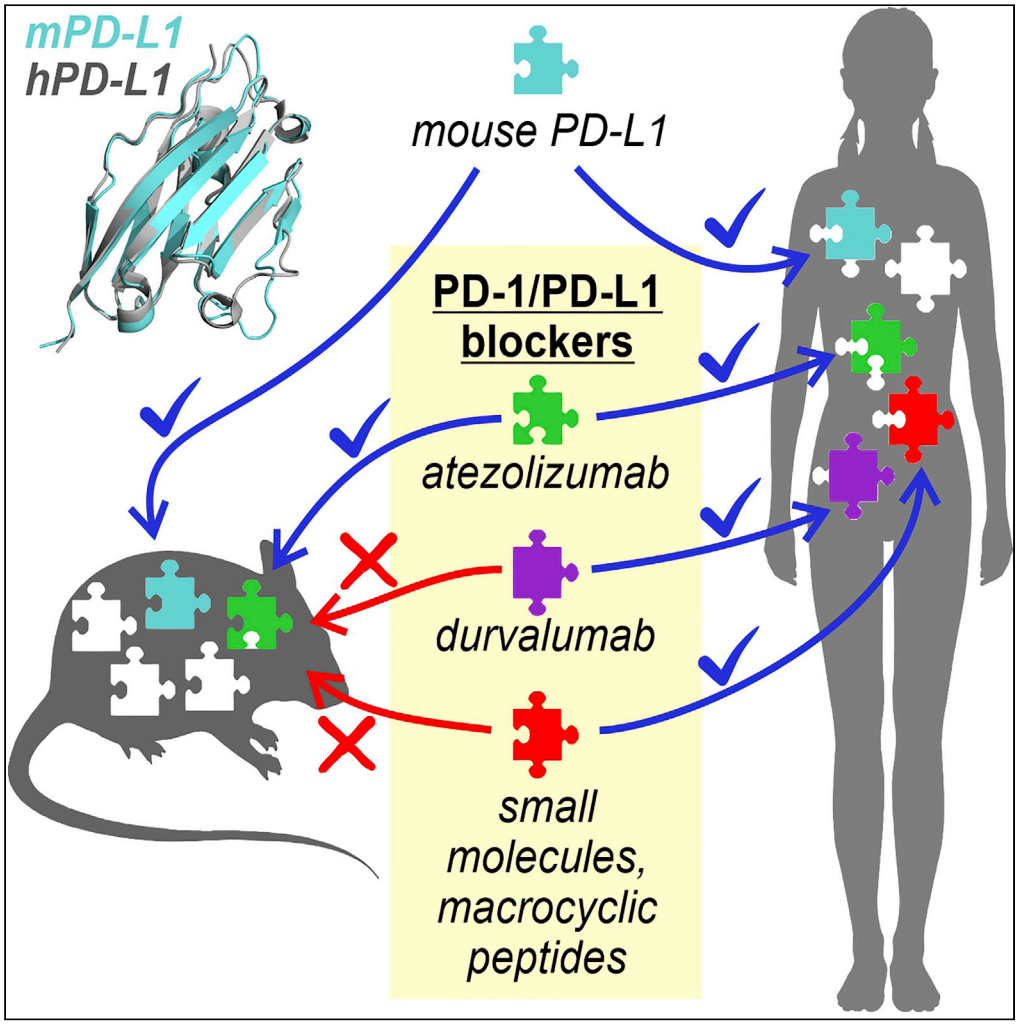

Katarzyna Magiera-Mularz, Justyna Kocik, Bogdan Musielak, ..., Maciej Siedlar, Tad A. Holak, Lukasz Skalniak

k.magiera@uj.edu.pl (K.M.-M.)
lukasz.skalniak@uj.edu.pl (L.S.)

Highlights

Mouse (*m*) PD-L1 interacts with human (*h*) PD-1 and inhibits human Jurkat T cells

Small molecule and macrocyclic peptide inhibitors of *h*PD-L1 do not bind to *m*PD-L1

Atezolizumab but not durvalumab binds and blocks mouse PD-L1

Magiera-Mularz et al., iScience *24*, 101960
January 22, 2021
https://doi.org/10.1016/j.isci.2020.101960

iScience

CellPress
OPEN ACCESS

Article

Human and mouse PD-L1: similar molecular structure, but different druggability profiles

Katarzyna Magiera-Mularz,[1,4,*] Justyna Kocik,[1,4] Bogdan Musielak,[1] Jacek Plewka,[1] Dominik Sala,[1] Monika Machula,[1] Przemyslaw Grudnik,[2] Malgorzata Hajduk,[3] Marcin Czepiel,[3] Maciej Siedlar,[3] Tad A. Holak,[1] and Lukasz Skalniak[1,5,*]

Summary

In the development of PD-L1-blocking therapeutics, it is essential to transfer initial *in vitro* findings into proper *in vivo* animal models. Classical immunocompetent mice are attractive due to high accessibility and low experimental costs. However, it is unknown whether inter-species differences in PD-L1 sequence and structure would allow for human-mouse cross applications. Here, we disclose the first structure of the mouse (*m*) PD-L1 and analyze its similarity to the human (*h*) PD-L1. We show that *m*PD-L1 interacts with *h*PD-1 and provides a negative signal toward activated Jurkat T cells. We also show major differences in druggability between the *h*PD-L1 and *m*PD-L1 using therapeutic antibodies, a macrocyclic peptide, and small molecules. Our study indicates that while the amino acid sequence is well conserved between the *h*PD-L1 and *m*PD-L1 and overall structures are almost identical, crucial differences determine the interaction with anti-PD-L1 agents, that cannot be easily predicted *in silico*.

Introduction

Tumor cells demonstrate tumor-specific antigens that facilitate the recognition by immune cells, provide the activation of the immune system, and enable the elimination of transformed cells. Immune checkpoint receptors play a crucial role in maintaining physiological T cell homeostasis, but also constitute a major factor in the escape of tumor cells from immune surveillance. The expression of immune checkpoint proteins allows for cancer progression by providing inhibitory circuits toward tumor-reactive T cells (Friedl and Wolf, 2003; Topalian et al., 2015; Zitvogel et al., 2006).

Programmed cell death receptor 1 (PD-1, CD279), together with its ligand, PD-L1 (CD274, B7-H1), constitutes one of the most important immune checkpoints as therapeutic targets (Azuma et al., 2008; Francisco et al., 2009; Zhang et al., 2009). Accordingly, over the past few years cancer immunotherapies based on therapeutic antibodies that block either the PD-1 receptor expressed on effector cells of the immune system or PD-L1 on tumor cells or in the tumor microenvironment, have revolutionized the approach to cancer treatment (Hoos, 2016) and provided a positive therapeutic outcome in a significant subset of patients (Chae et al., 2018; Herbst et al., 2014; Larkin et al., 2019). Until now, six monoclonal antibodies targeting PD-1/PD-L1 interaction have been approved by the US Food and Drug Administration (FDA) (Lee et al., 2019).

The clinical success of antibody-driven therapies evoked a great pursuit for the discovery of small-molecule- and peptide-based PD-1/PD-L1 blockers (Guzik et al., 2019; Shaabani et al., 2018; Yang and Hu, 2019), which would reduce the costs of therapies and possibly allow for *per os* drug delivery (Hansel et al., 2010). Transferring drug candidates through *in vivo* experiments with the use of appropriate animal models is a fundamental process that allows for the evaluation of the therapeutic index and progression to clinical trials. While in the classical experimental chemotherapy and targeted therapy approaches immunodeficient mice bearing human cell xenografts are largely acceptable models, immunotherapy-directed studies require the co-existence of the functional immune system and immune-compatible tumor implants. This can be achieved either by using syngeneic mouse models (fully mouse systems) or by introducing

[1]Department of Organic Chemistry, Faculty of Chemistry, Jagiellonian University, Gronostajowa 2, 30-387 Krakow, Poland

[2]Malopolska Center of Biotechnology Jagiellonian University, Gronostajowa 7, 30-387 Krakow, Poland

[3]Department of Clinical Immunology, Institute of Pediatrics, Jagiellonian University Medical College, Wielicka 265, 30-663 Krakow, Poland

[4]These authors contributed equally

[5]Lead contact

*Correspondence: k.magiera@uj.edu.pl (K.M.-M.), lukasz.skalniak@uj.edu.pl (L.S.)

https://doi.org/10.1016/j.isci.2020.101960

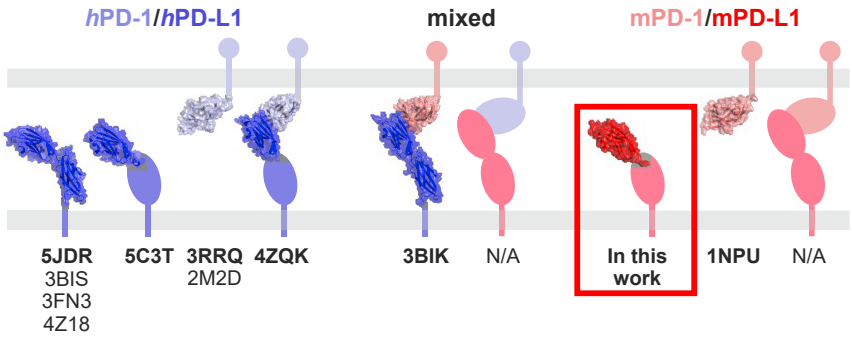

Figure 1. The available molecular structures that comprise either the human or mouse PD-1 or PD-L1 proteins alone or complexes thereof

effortful humanized animals that provide the interaction between human target cells, or at least human molecular targets (De La Rochere et al., 2018; Zitvogel et al., 2016). Importantly, the choice of a proper model has to be made rationally following the analysis of the druggability of the molecular target of human and mouse origins. However, structural details on the mouse PD-L1 (*m*PD-L1), as well as *in vitro* methods for the prediction and verification of its applicability in particular immuno-oncology projects are still missing.

Here, for the first time, we deliver the structure of the PD-1-binding domain of *m*PD-L1. Next we show that alike its human counterpart, *m*PD-L1 is able to interact with the *hPD*-1 and provides a functional immune checkpoint for the activated human Jurkat T cells. Then, we check the druggability of the *h*/*h* and *h*/*m* PD-1/PD-L1 immune checkpoints with representative PD-L1-targeting small molecules and a macrocyclic peptide. We also demonstrate the use of a new cell-based assay that may guide the selection between the classical mouse models and humanized mouse models for pre-clinical testing of the activity of experimental PD-L1-targeting drugs.

Results

The overall structure of the mouse Apo-PD-L1

Several molecular structures of human PD-1 and PD-L1 proteins have been delivered in recent years (Figure 1). Additionally, the structure of the mouse PD-1 was also disclosed. While it was assumed that PD-L1 of mouse and human origins should share a high structural similarity, experimental proofs were missing. To fill this gap, we crystallized the N-terminal PD-1-binding domain of the *m*PD-L1 protein (amino acids 19-134). The obtained crystal diffracted to the 2.5 Å resolution and contained 10 protein molecules in the asymmetric unit (Figure S1A). The crystal packing did not suggest oligomerization of the V-type domain of *m*PD-L1, consistent with its one-domain human homolog structure reported previously (Zak et al., 2015). Protein chains were arranged into two similar symmetric subunits formed by the one central PD-L1 molecule and four molecules located around the center. The subunits are contacted by the four outer PD-L1 molecules, but not the central one. Therefore, an empty core is formed in the center of the asymmetric unit (Figure S1A). The unit exhibits a pseudo-two-fold rotational symmetry around an axis parallel to the empty core.

Similarly to the human PD-L1, the mouse protein shows the immunoglobulin-variable type topology with canonical two layers of antiparallel β-sheets (ABED and GFCC′C″, Figure 2A). Protein chains are well visible in electron density except for the two variable loops: BC (Val44-Leu47) and C″D (Leu74-Ser79). The superposition of *m*PD-L1 structures from ten copies within a single crystal unit showed only slight structural deviations in protein chains, with larger shifts in the variable loop regions (Figure S1B).

The apo-*h*PD-L1 (PDB: 5C3T) and *m*PD-L1 structures demonstrate the same general fold of the chains with root-mean-square deviation of 0.68 Å among C-alpha carbon atoms. Several significant differences within the tertiary structures are noticeable, mostly in the variable loop regions (BC and C″D loops), which are distant from the classical inhibitor-binding site and do not participate in the PD-1/PD-L1 complex formation (Figure 2A). However, the arrangement of the BC loop is debatable as a result of the flexible nature of

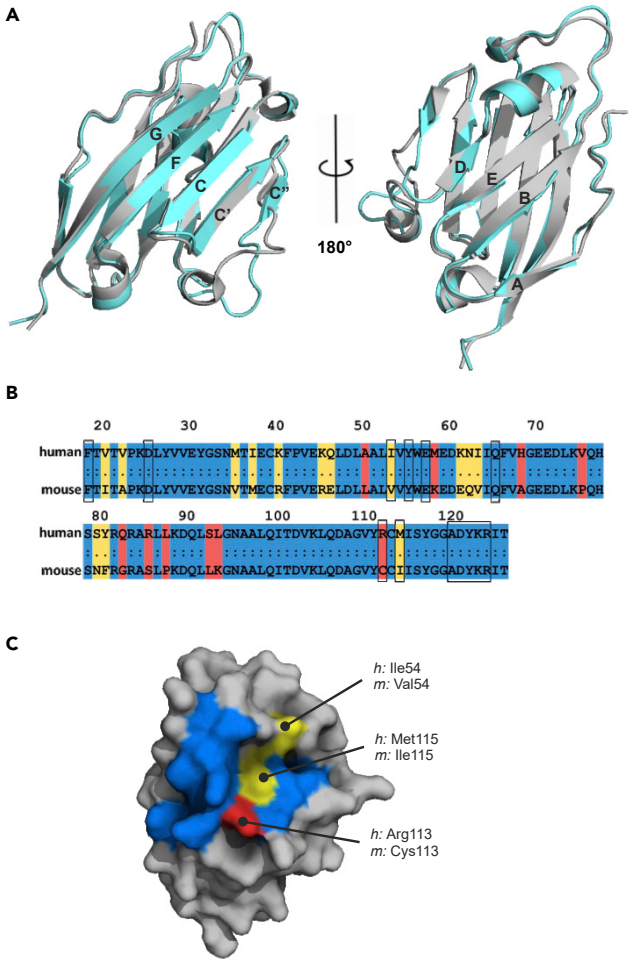

Figure 2. The comparison of structure and sequence of PD-1-binding domains of human and mouse PD-L1 proteins

(A) The superposition of PD-1-binding domains of the human (gray, PDB: 5C3T) and mouse (cyan, PDB: 6SRU) PD-L1 proteins.

Canonical Ig-strand designations ABED and GFCC'C" are used (Zak et al., 2017).

(B) Protein sequence alignment of PD-1-binding domains of human and mouse PD-L1. Conserved residues are colored blue, minor changes – yellow, significant differences – red. Black boxes indicate amino acids of *h*PD-L1 engaged in the interaction with *h*PD-1, and corresponding amino acids of *m*PD-L1.

(C) Human PD-L1 structure with the surface representation of the *h*PD-L1/*m*PD-L1 sequence alignment within the interaction surface with the *h*PD-1, colored according to (B).

See also Figures S1 and S2.

this poorly structured region, causing many conformations or incomplete electron density for this fragment in different chains of the *m*PD-L1 structure (Figure S1B).

Mouse PD-L1 interacts with human PD-1

The PD-1-binding domain of the human PD-L1 (Ig V-type PD-L1 domain 19-127 amino acids) shows a relatively low overall sequence identity (69.4%) and similarity (87.6%) with the mouse protein (Figure 2B). However, a detailed sequence and structure comparison within the *h*PD-1/*h*PD-L1 interaction surface demonstrates a similar arrangement of Phe19, Ala121, Asp122, Tyr123, Lys124, and Arg125 between human and mouse PD-L1 (Figures 2B and 2C). The most significant spatial rearrangement of the key amino acid within this region is a dislocation of the Tyr56 sidechain in the *m*PD-L1 structure compared to the *h*PD-L1 structure, resulting in ~7 Å displacement of its terminal hydroxylic group (Figure S2). In addition, three amino acids involved in the formation of the *h*PD-1/*h*PD-L1 complex (Ile54, Arg113, and Met115) are changed

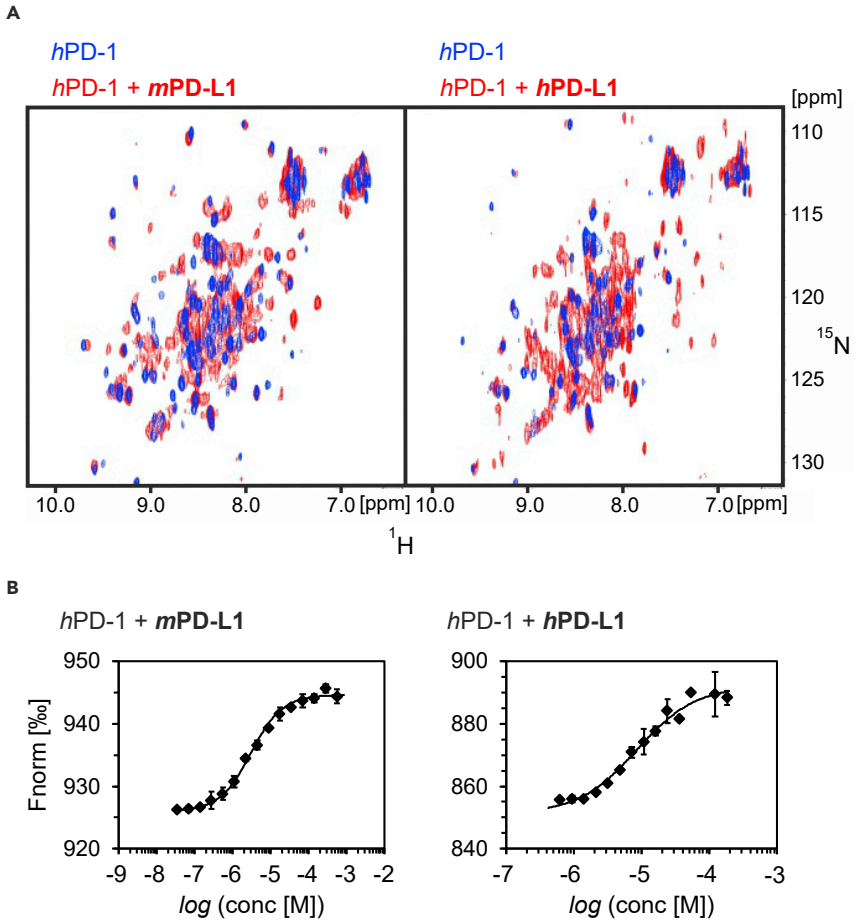

Figure 3. Mouse PD-L1 interacts with the human PD-1

(A) The superposition of ^{1}H-^{15}N HMQC spectra of the *h*PD-1 (blue) and its complex with PD-L1 (red) of either the mouse (*m*PD-L1, left panel) or human (*h*PD-L1, right panel) origin. In both 2D spectra, PD-1/PD-L1 complex formation is evidenced by the broadening of resonance signals caused by increased transverse relaxation.

(B) The interaction of *h*PD-1 with either *m*PD-L1 (left) or *h*PD-L1 (right) was tested with MicroScale Thermophoresis (MST) binding assay. The resulting K_D value for *h*PD-1/*h*PD-L1 was 11.9 $\pm$ 2.8 μM, and 3.2 $\pm$ 0.2 μM for *h*PD-1/*m*PD-L1. All MST measurements were performed in two independent dilution series. Errors for measurement points are reported as standard deviations.

in the *m*PD-L1 sequence to Val54, Cys113, and Ile115, respectively (Figure 2C). Among these, the Arg113/Cys113 mismatch seems the most prominent causing the inability of the salt bridge formation between *h*PD-1 and *m*PD-L1 (Zak et al., 2015). Altogether, these alterations might be sufficient to prevent the interaction of *m*PD-L1 with *h*PD-1 protein.

To verify the binding of *m*PD-L1 with *h*PD-1 nuclear magnetic resonance (NMR) spectroscopy was employed. For this, the 2D antagonist-nduced dissociation assay (AIDA) (Krajewski et al., 2007), used previously to assess the interaction of small molecules with *h*PD-L1 (Skalniak et al., 2017) was utilized. In the AIDA-NMR assay, the ^{15}N-labeled *h*PD-1 is monitored in the ^{1}H-^{15}N heteronuclear multiple quantum correlation (HMQC) NMR experiment. Partial shifting and broadening of HMQC signals upon addition of the ^{14}N PD-L1 indicate the formation of PD-1/PD-L1 complex, while no change implies a lack of this protein-protein interaction. In the experiment, both the human and mouse PD-L1 formed the complex with *h*PD-1 (Figure 3A). Compared to the spectrum of *h*PD-L1/*h*PD-1 complex, ^{1}H-^{15}N cross-peaks signals are less broadened and sharper for the *m*PD-L1/*h*PD-1 complex, which indicates a higher value of the dissociation constant of *m*PD-L1/*h*PD-1 than for *h*PD-L1/*h*PD-1 complex (Figure 3A).

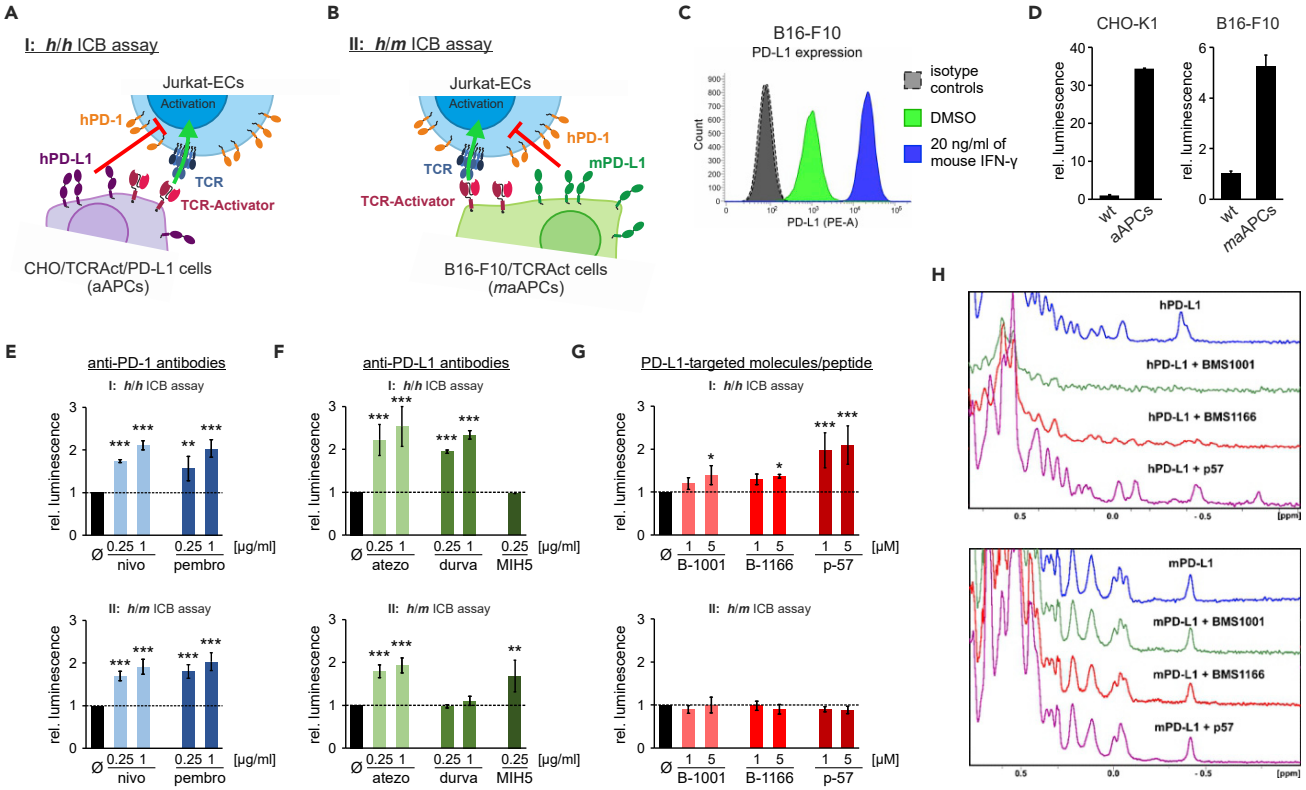

Figure 4. The *h/m* and *h/h* PD-1/PD-L1 checkpoint functionally impair the activation of Jurkat T cells but have distinct druggability profiles

(A) A schematic representation of the immune checkpoint blockade (ICB) assay, that provides the *h/h PD-1/PD-L1 immune checkpoint* (*h*/*h*ICB).

(B) A schematic representation of the ICB assay, that provides the *h/m PD-1/PD-L1 immune checkpoint*(*h*/*m*ICB).

(C) Flow cytometry analysis of the expression of *m*PD-L1 on the surface of *ma*APCs, either at the basal state (green) or following the treatment with 20 ng/mL of mouse IFN-γ (blue).

(D) The activation of Jurkat T cells by the cells expressing TCR-Activator compared to parental (wt) cells.

(E–G) The activity of: (E), anti-PD-1 therapeutic antibodies (nivo: nivolumab, pembro: pembrolizumab), (F), anti-PD-L1 antibodies (atezo: atezolizumab, durva: durvalumab, MIH5: control anti-mouse PD-L1 antibody), and (G) PD-L1-targeted small molecules (B-1001: BMS-1001, B-1166: BMS-1166) and the macrocyclic peptide (p-57) in *h*/*h*ICB and *h*/*m*ICB assays. The graphs show luminescence values relative to untreated control cells (black bars) and reflect the relative activation of Jurkat T cells following the depicted treatments. The results are mean ± SD values from three independent experiments. Statistical analysis was performed using ANOVA with Fisher's post-hoc test for pairwise comparison with untreated control cells: *, $p < 0.05$, **, $p < 0.01$, ***, $p < 0.001$.

(H) NMR analysis of the interaction of small molecules and the peptide with *h*PD-L1 (top) and *m*PD-L1 (bottom). Aliphatic regions of ^{1}H NMR spectra of the human (top) and mouse (bottom) PD-L1, alone or in the presence of the indicated molecules are shown. The colors depict ^{1}H NMR spectra of apo-PD-L1 proteins (blue), and PD-L1 proteins overtitrated with BMS-1001 (green, 1:2 molar ratio), BMS-1166 (red, 1:2 molar ratio), and the peptide-57 (purple, 1:1 molar ratio). The linewidth broadening of the NMR signals and changes in the aliphatic region are visible only in *h*PD-L1 spectra implying no interactions between *m*PD-L1 and BMS compounds or peptide-57.

See also Figures S3 and S4.

The binding affinity (K_D) between either the *m*PD-L1 or *h*PD-L1 and *h*PD-1 was further determined using MicroScale Thermophoresis (MST) assay. *h*PD-1 was covalently labeled with a fluorophore to allow for monitoring of the thermal stability of the target protein. The interaction of the labeled *h*PD-1 with its ligand, such as PD-L1, changes the stability of the protein observed as a change of the Fnorm [‰] parameter. Labeled *h*PD-1 was incubated with increasing concentrations of unlabeled *h*PD-L1 or *m*PD-L1. For both proteins a dose-dependent change in the Fnorm [‰] value was observed, indicating the interaction between them (Figure 3B). Resulting data points from two independent dilution series were fitted with K_D model resulting in K_D values of 11.9 ± 2.8 μM for the *h*PD-1/*h*PD-L1 interaction and 3.2 ± 0.2 μM for the *h*PD-1/*m*PD-L1 (Figure 3B).

Mouse PD-L1 forms a functional immune checkpoint with human PD-1

Given that *m*PD-L1 interacts with the *h*PD-1 protein, we were interested in whether this interaction may provide a functional immune checkpoint, as in the case of the *h*PD-L1/*h*PD-1. For this, a new setup of the

previously utilized immune checkpoint blockade (ICB, otherwise called *h*/*h*ICB) assay (Magiera-Mularz et al., 2017; Skalniak et al., 2017) was prepared, in which the CHO-based artificial antigen-presenting cells (CHO/TCRAct/PD-L1, otherwise called aAPCs), which expose the hPD-L1 protein to the Jurkat T cell-like effector cells (Jurkat-ECs) (Figure 4A), were substituted with mouse aAPCs (B16-F10/TCRAct, otherwise called *m*aAPCs), prepared by overexpressing TCR-Activator on the surface of B16-F10 cells (Figure 4B). To assure a high expression of *m*PD-L1, *m*aAPCs were pre-treated for 48 hr with 20 ng/mL of mouse IFN-γ (Figure 4C). Such a setup, herein called the *h*/*m*ICB assay, provides the TCR-dependent activation of the Jurkat-ECs and presentation of endogenous *m*PD-L1 expressed by the B16-F10 cells.

The exposition of Jurkat-ECs to either aAPCs or *m*aAPCs resulted in strong TCR-dependent activation of ECs compared to Jurkat-ECs exposed to initial CHO-K1 or B16-F10 cells, as monitored by the NFAT-mediated expression of luciferase (Figure 4D). In both setups, the addition of anti-PD-1 therapeutic antibodies, nivolumab or pembrolizumab, resulted in a significant increase in the activation of Jurkat-ECs suggesting the functional activity of both the *h*PD-1/*h*PD-L1 and the *h*PD-1/*m*PD-L1 immune checkpoints (Figure 4E).

Mouse and human PD-L1 present different profiles of druggability with therapeutic antibodies, BMS small molecules, and peptide-57

To check the species-dependent effects of the molecules designed to block PD-L1 for therapeutic purposes, the original *h*/*h*ICB assay and the *h*/*m*ICB assay were performed in the presence of five molecules, belonging to three distinct classes: the monoclonal antibodies (atezolizumab and durvalumab), small molecules (**BMS-1001** and **BMS-1166**), and peptides (**peptide-57**). The dose-dependent activities of these compounds were presented in our previous studies (Magiera-Mularz et al., 2017; Skalniak et al., 2017). As expected, all the compounds increased the activation of Jurkat-ECs in the standard *h*/*h*ICB assay setup, suggesting a successful blockade of the *h*PD-1/*h*PD-L1 immune checkpoint (Figures 4F and 4G, upper panels). In the assay, both FDA-approved antibodies presented the highest potency, followed by **peptide-57**. Small molecules **BMS-1001** and **BMS-1166** presented only low activity, which is in agreement with our previous report (Skalniak et al., 2017). MIH5, which is a mouse-specific anti-PD-L1 antibody, did not interfere with the *h*PD-1/*h*PD-L1 immune checkpoint (Figure 4F, upper panel).

Interestingly, neither the peptide nor small molecules were able to provide the blockade of the *h*PD-1/*m*PD-L1 immune checkpoint (Figure 4G, lower panel). The control anti-mouse PD-L1 MIH5 antibody was able to reactivate Jurkat-ECs blocked by the *m*PD-L1 (Figure 4F, lower panel). To verify these findings, a ^{1}H NMR experiment was performed with the use of either the mouse or human PD-L1. The experiment confirmed the binding of **BMS-1001**, **BMS-1166**, and **peptide-57** to the *h*PD-L1, as evidenced by the changes in the NMR spectra (Figure 4H). When the *m*PD-L1 was used, no changes in the corresponding spectra were observed, indicating no interaction of these agents with the mouse PD-L1 (Figure 4H). Similar specificity toward the *h*PD-L1 was observed in ^{1}H NMR experiments for four other biphenyl-based BMS compounds, i.e. **BMS-37**, **BMS-200**, **BMS-202**, and **BMS-242**. We have shown before that these compounds bind to *h*PD-L1 (Guzik et al., 2017; Skalniak et al., 2017; Zak et al., 2016). The compounds bound to *h*PD-L1, but no binding to the *m*PD-L1 was observed (Figure S3). This was further confirmed by the MST assay, where neither **BMS-1166** nor **peptide-57** was able to interact with *m*PD-L1 (Figure S4).

Out of the tested therapeutic antibodies, only atezolizumab was able to increase the activation of Jurkat T cell-like effector cells, suppressed by the *m*PD-L1 protein (Figure 4F, lower panel). Durvalumab was inactive against the *m*PD-L1.

Atezolizumab, but not durvalumab displays anti-cancer properties in an immunocompetent mouse model

Our cell-based model predicts the differences in binding of PD-L1-targeting molecules to the *m*PD-L1 compared to the intended molecular target, which is *h*PD-L1. To verify the reliability of this prediction, the activity of the two anti-PD-L1 therapeutic antibodies, atezolizumab and durvalumab, toward the mouse PD-L1 was further analyzed.

First, binding of the antibodies to the human and mouse PD-L1 was verified using the MST assay. Fluorescently labeled *h*PD-L1 and *m*PD-L1 were incubated with increasing concentrations of antibodies. MIH1 and MIH5 antibodies were used as positive controls for *h*PD-L1 and *m*PD-L1, respectively. All of the anti-human antibodies, MIH1, atezolizumab, and durvalumab, interacted with *h*PD-L1 (Figure 5A). The determined K_D

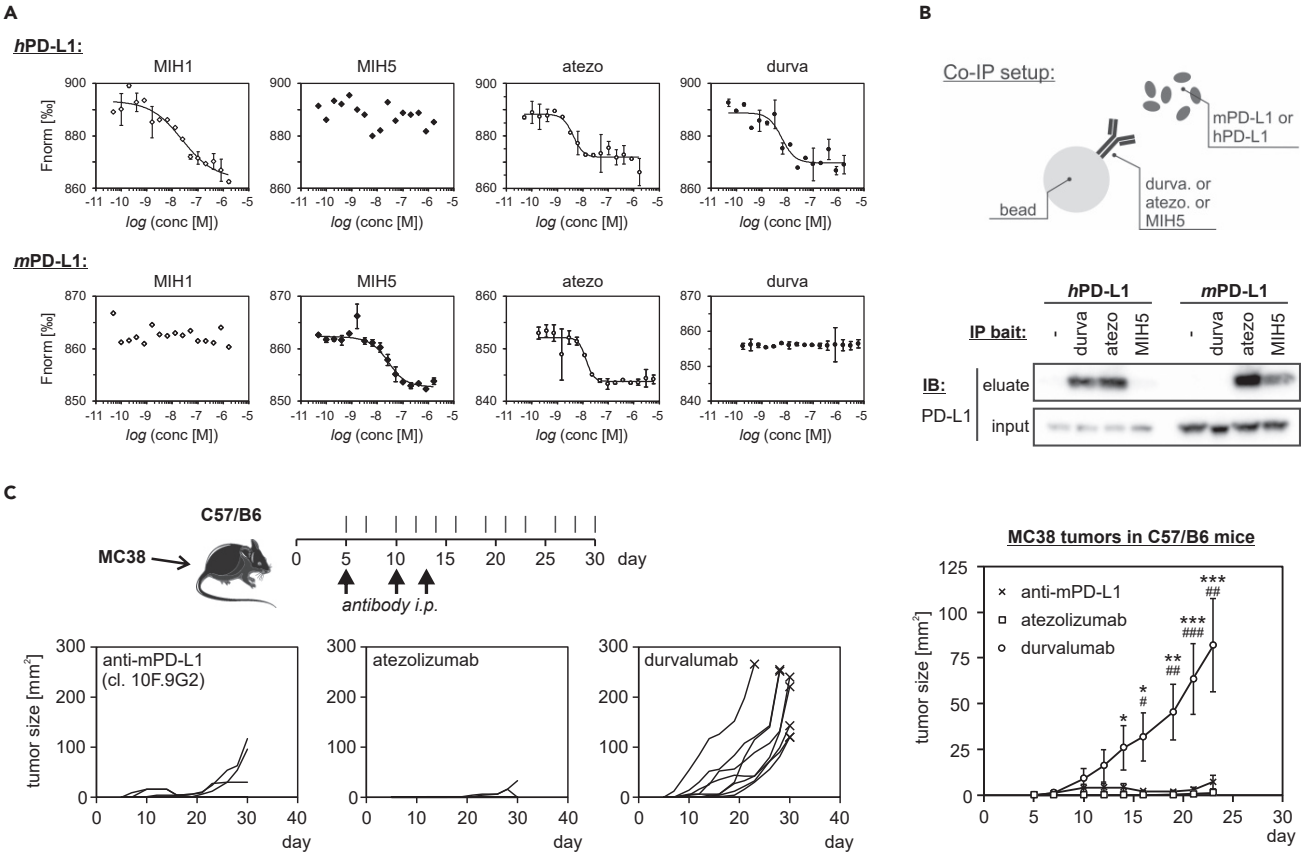

Figure 5. The activity of durvalumab and atezolizumab toward *h*PD-L1 and *m*PD-L1

(A) The interaction of either *h*PD-L1 (upper panels), or *m*PD-L1 (lower panels) with anti-PD-L1 antibodies was tested with MicroScale Thermophoresis (MST) binding assay. The antibodies used were: MIH1: positive control anti-*h*PD-L1, MIH5: positive control anti-*m*PD-L1, atezo: atezolizumab, durva: durvalumab. All MST measurements were performed in two independent dilution series. Errors for measurement points are reported as standard deviations.

(B) Co-immunoprecipitation assay performed with the use of beads coated with the indicated anti-PD-L1 antibodies (bait), incubated with either *h*PD-L1, or *m*PD-L1 (prey). The figure shows data representative for three independent experiments. See also Figure S5.

(C) MC38 tumor growth control experiment. C57/B6 mice were given 5 × 10^5 MC38 cells s.c. and treated on days 5, 10, and 13 with anti-PD-L1 (10F.9G2; n = 9), atezolizumab (n = 9), or durvalumab (n = 9). Tumors were measured every 2-3 days starting on day 5. The three small plots show tumor growth data for all animals separately. The plot on the right-hand side presents mean ± SEM values from all animals within each group (n = 9). For statistics, ANOVA was performed with Holm post-hoc test; durva vs. 10F.9G2: #, $p < 0.05$, ##, $p < 0.01$, ###, $p < 0.001$; durva vs. atezo: *, $p < 0.05$, **, $p < 0.01$, ***, $p < 0.001$.

values were: 24.5 ± 13.6 nM for MIH1, 4.2 ± 0.9 nM for atezolizumab, and 5.9 ± 2.1 nM for durvalumab. The anti-mouse MIH5 antibody showed no binding to *h*PD-L1. In contrast, MIH1 presented no binding to the *m*PD-L1, while the binding of MIH5 was well visible (K_D = 13.4 ± 4.4 nM). Comparable binding affinity was observed for atezolizumab (K_D = 13.4 ± 2.3 nM), while durvalumab failed to interact with *m*PD-L1 (Figure 5A).

Similar species-related target specificity was determined in a co-immunoprecipitation assay, where either mouse or human PD-L1 (prey) was precipitated with beads coated with durvalumab, atezolizumab, or MIH5 as an anti-*m*PD-L1 positive control (bait). In the experiment, both durvalumab and atezolizumab showed binding to the *h*PD-L1 protein, while from this pair only atezolizumab was able to precipitate *m*PD-L1 (Figures 5B and S5). The control anti-mouse antibody MIH5 precipitated only the *m*PD-L1, but not the *h*PD-L1 (Figure 5B).

Finally, to validate the difference in activities of atezolizumab and durvalumab toward *m*PD-L1, a mouse tumor growth control experiment was performed. Immunocompetent C57/B6 mice implanted subcutaneously with the syngeneic MC38 cells were treated with atezolizumab, durvalumab, or a positive control anti-PD-L1 mouse antibody (clone 10F.9G2), and the tumor size was monitored for 25 days following the start of

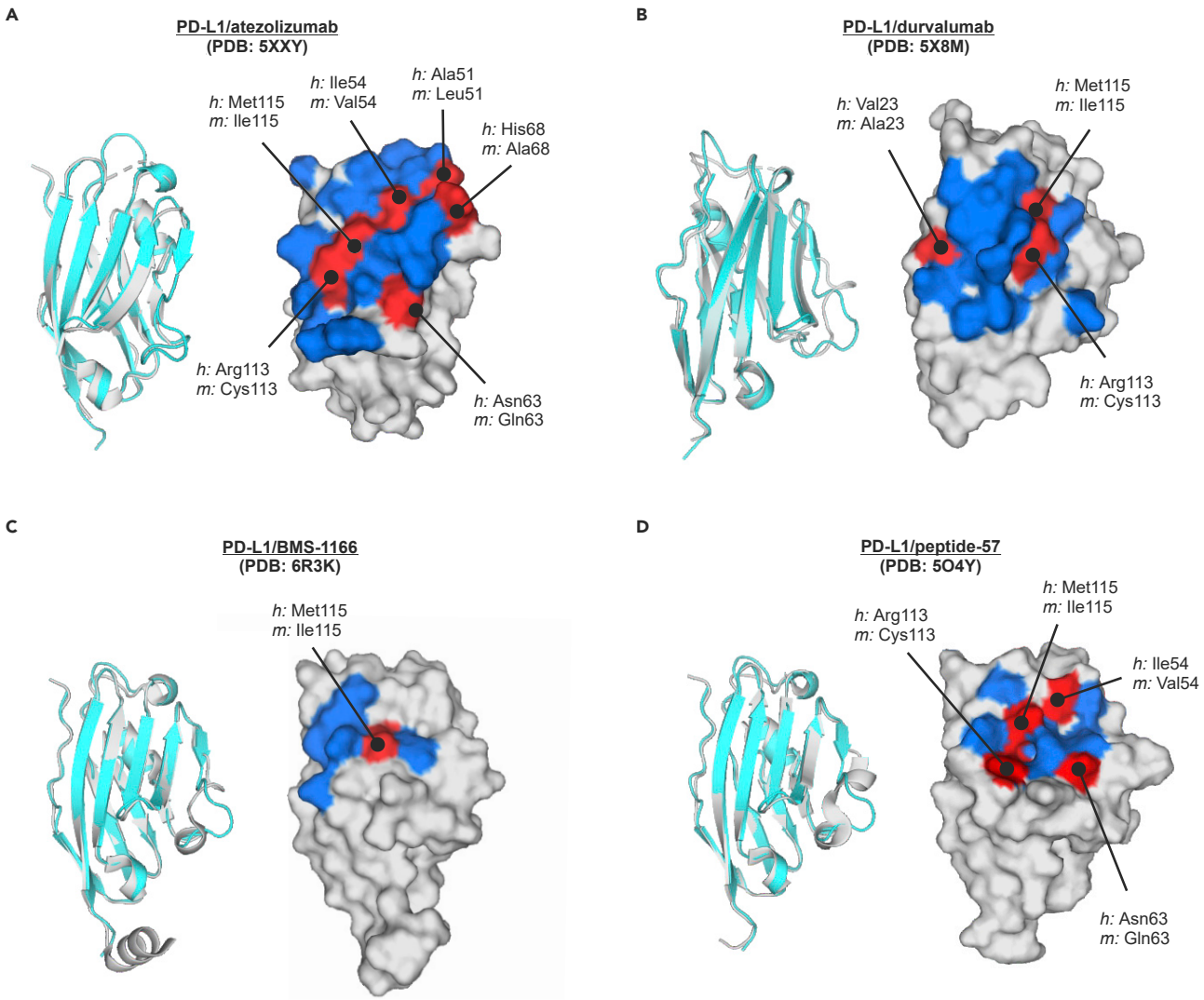

Figure 6. The analysis of amino acid composition of the interaction surface of PD-L1 with its blocking agents

The comparison of the amino acid compositions of *h*PD-L1 and corresponding amino acids of the *m*PD-L1 at the interfaces of *h*PD-L1 with atezolizumab (A), durvalumab (B), BMS-1166 (C), and peptide-57 (D). The residues conserved between *h*PD-L1 and *m*PD-L1 are colored blue on surface representations, while the differences determined from the sequence alignment are colored red and pointed with a line. Gray surfaces represent amino acids that are apart from interaction surfaces. Structural alignments of the human (gray) and mouse (cyan) PD-L1 are shown as cartoon representations to define the orientation of the corresponding surface representations of *h*PD-L1 from given crystal structures. See also Figure S6 and Table S1.

the treatment (Figure 5C). All animals treated with atezolizumab were clear from the tumors throughout the experiment (9/9). In contrast, almost all animals (8/9) treated with durvalumab developed the tumors that reached an average size of 80 mm^2 on day 23 of the experiment (Figure 5C). The treatment with the *in vivo*-dedicated anti-*m*PD-L1 antibody clone 10F.9G2 also allowed for a good inhibition of the growth of MC38 tumors in C57/B6 mice, however, some animals (3/9) started to develop tumors after two weeks following the start of the treatment (Figure 5C).

Molecular structure and amino acid sequence do not predict the druggability of the mPD-L1

To visualize the observed differences in the druggability of *h*PD-L1 and *m*PD-L1 with therapeutic antibodies, small molecules, and the peptide, the amino acid composition of PD-L1/drug interaction surfaces of *h*PD-L1 was determined based on appropriate co-crystal structures. The amino acid composition of each

of the binding sites on the *h*PD-L1 was then compared to the corresponding amino acids of the *m*PD-L1 to define the residues that might underlie the observed differences in druggability.

The atezolizumab epitope within *h*PD-L1, determined from the crystal structure PDB: 5XXY, consists of 23 residues located in the CC'FG β-sheet, and loops BC, CC', C'C", and FG (Lee et al., 2017). Among these 23 residues, 6 are modified in the sequence of mouse PD-L1 (Figure 6A, Table S1). Durvalumab/*h*PD-L1 binding interface (from PDB: 5X8M) occupies a narrower area and is composed of 16 residues located in the strands C, F, and G and the CC' loop, wherein 3 amino acids of the epitope are different when comparing mouse and human PD-L1 sequences (Figures 6B and Table S1). The shared epitope region for these two antibodies contains 10 residues (Tyr56, Glu58, Glu60, Asp61, Val111, Arg113, Met115, Ala121, Tyr123, and Arg125), and includes two amino acids modified between human and mouse protein (Arg113/Cys113, and Met115/Ile115).

The interaction site of **BMS-1166** and *h*PD-L1, determined from the crystal structure PDB: 6R3K consists of 8 PD-L1 residues, i.e. Ile54, Tyr56, Met115, Ala121, Asp122, Tyr123, Lys124, and Arg125 (Skalniak et al., 2017). Two out of these residues, namely Ile54 and Met115, differ between the two species, while the remaining six are the same (Figure 6C and Table S1). The binding site of **peptide-57** at the surface of *h*PD-L1 is composed of 10 amino acids, as predicted from the structure PDB: 5O4Y. Four out of these amino acids are different in the sequence of *m*PD-L1. These alterations are Ile54/Val54, Asn63/Gln63, Arg113/Cys113, and Met115/Ile115 (Figure 6D and Table S1).

Possible molecular determinants of the species-specificity of the BMS compounds

As we have previously shown, the complexes of BMS small molecules (**BMS-8**, **BMS-37**, **BMS-200**, **BMS-202**, **BMS-1001**, and **BMS-1166**) with *h*PD-L1 are stabilized mostly by interactions of the compounds with *h*PD-L1 residues Phe19, Tyr56, Met115, Ala121, Asp122, Tyr123, Lys124, and Arg125 (Guzik et al., 2017; Skalniak et al., 2017; Zak et al., 2016). Surprisingly, these amino acids occur both in human and mouse PD-L1 sequences, except for the Met115, which is replaced by Ile115 residue in the mouse protein sequence (Figures 1B and 6C). Although the sidechains of Met115 in *h*PD-L1 and Ile115 in *m*PD-L1 overlay relatively well in the superposed structures, this replacement introduces a branched aliphatic chain to the already crowded space. Therefore, the isoleucine chain can sterically collide with the biphenyl moiety of BMS-compounds (C-C distances: 2.4 and 2.6 Å), leading to failure of the binding of the biphenyl-based inhibitors to the murine protein (Figure S6).

The second notable structural alteration is the movement of the Tyr56 sidechain, which is the largest rearrangement observed within the interaction surface between PD-L1 and **BMS-1166** when comparing the structures of apo *h*PD-L1 with apo *m*PD-L1. However, in our previous studies, we showed the Tyr56 sidechain rearrangement induced by the interaction of *h*PD-L1 with different BMS compounds. An overlay of the *m*PD-L1 and *h*PD-L1/**BMS-1166** structures shows that the rearrangement of Tyr56 necessary for binding of **BMS-1166** is prohibited in the *m*PD-L1 structure by the proximity of the Gln63 sidechain, which would also need to move out to allow for the inhibitor interaction. However, the arrangement of the strands seems to provide the space required for the reorganization of the sidechains. Therefore, the spatial arrangement of Tyr56 and Gln63 cannot be considered as the sole source for the inactivity of **BMS-1001** and **BMS-1166** toward *m*PD-L1. To check our hypothesis, we additionally tested the affinity of **BMS-37**, **BMS-202**, and **BMS-242** which are deprived of the 1,4-dioxane moiety and do not require large movement of Tyr56 upon binding. Determination of binding of **BMS-37**, **BMS-202**, and **BMS-242** to *m*PD-L1 was carried out, again, using the ^{1}H NMR spectroscopy. In the resulting 1D proton spectra the linewidth broadening of the NMR lines of *m*PD-L1 was not observed, confirming a lack of interaction between these BMS compounds and *m*PD-L1.

Discussion

The structural characterization of the PD-1/PD-L1 immune checkpoint proteins is now extensive [19]. By now, crystal structures of the extracellular parts of the human PD-L1 containing either a single PD-1-binding domain (Zak et al., 2015) or both Ig-like domains (Chen et al., 2010; Lin et al., 2008; Zhang et al., 2017), were resolved (Figure 1). Likewise, the structures of extracellular domains of the mouse and human PD-1 proteins have been described (Cheng et al., 2013; Zhang et al., 2004). The crystal structure of the *m*PD-1/*m*PD-L2 complex was published in 2008 (Lázár-Molnár et al., 2008), likewise the mixed structure of *m*PD-1 and *h*PD-L1 (Lin et al., 2008). Next, the structure of a fully human PD-1/PD-L1 complex led to the

characterization of hot-spot pockets required for the inhibition of *h*PD-1/*h*PD-L1 complex formation (Zak et al., 2015). More recently, the crystal structure of hPD-1/hPD-L2 was also published (Tang and Kim, 2019).

Out of the mouse and human PD-1/PD-L1 proteins, only the structure of the *m*PD-L1 was missing. In this paper, we fill this gap by providing the 2.5 Å-resolution crystal structure of a PD-1-binding domain of the mouse PD-L1 protein. We carried out herein a detailed structural comparison of *m*PD-L1 and *h*PD-L1 indicating their high structural similarity. We also show that human and mouse PD-L1 share enough sequence homology to allow for the interaction of the *m*PD-L1 with the *h*PD-1 protein, forming a functional immune checkpoint. This hybrid immune checkpoint was shown to functionally impair TCR-mediated activation of the reporter human Jurkat T cell-like cells, as evidenced by the observed increased activation in the presence of PD-1 blocker, nivolumab, and some other PD-1/PD-L1-blocking antibodies.

The K_D of the interaction between *h*PD-1 and *h*PD-L1 determined in this study (11.9 $\pm$ 2.8 μM) was in close agreement with previous data (c.a. 8 μM) (Cheng et al., 2013; Magnez et al., 2017). Despite minor sequence differences, both the *h*PD-L1 and the *m*PD-L1 are able to interact with the *h*PD-1 with comparable affinity. We, therefore, decided to check whether the *m*PD-L1 could also be targeted with the molecules designed to target the *h*PD-L1. Such an analysis is of high importance, as it might allow for choosing simple immunocompetent mouse models bearing syngeneic tumors instead of the humanized animals for pre-clinical evaluation of the bioactivity of therapeutic molecules. To our surprise, neither BMS small molecules nor the cyclic **peptide-57** were able to interact with the *m*PD-L1, while the interaction with the *h*PD-L1 was confirmed by the experimental data. This is a crucial message as it indicates that a profound *in vitro* analysis of the druggability of the *m*PD-L1 with the tested compounds is required before investing resources and time into the experiments on non-humanized animals. Moreover, the comparative analysis of the sequences and structures of mouse and human PD-L1 indicates that there is unlikely a simple rule for predicting the interaction of the *h*PD-L1-targeting ligand with the *m*PD-L1. This is well exemplified by the analysis of the two therapeutic antibodies, atezolizumab, and durvalumab, as well as BMS compounds. For both of these antibodies, amino acid sequences within their binding sites on *h*PD-L1 comprise several mismatches with the corresponding sequence of the *m*PD-L1, i.e. 3 mismatches for durvalumab, and 6 for atezolizumab, two out of which overlap for both binding sites. Despite this, it was durvalumab that did not show any interaction with the *m*PD-L1. In contrast, atezolizumab was able to interact with the *m*PD-L1, block the *m*PD-L1/*h*PD-L1 immune checkpoint in a cell-based assay, and provide inhibition of the growth of mouse tumors in a syngeneic mouse model, where the *m*PD-L1/*m*PD-1 immune checkpoint is present. Notably, the expected binding surface on *m*PD-L1 that matches the surface on *h*PD-L1 is much larger for atezolizumab (17 amino acids) than for durvalumab (13 amino acids). This may be the reason for the observed activity of atezolizumab, but not durvalumab, toward the *m*PD-L1.

These days, the interest in the examination of *in vivo* activity of emerging antibody- and non-antibody-based inhibitors of PD-1/PD-L1 is clearly increasing. Recently, several studies aiming at the evaluation of the anti-cancer properties of the biphenyl-based small molecules were presented. In a subset of these studies, syngeneic mouse models are utilized. In 2019, Zhang and co-workers published their work on **BMS-202** nanoparticles injected intravenously into BALB/c mice bearing mouse mammary gland 4T1 tumors (Zhang et al., 2019). In 2020 Hu and collaborators claimed anti-tumor effects of **BMS-202** toward B16-F10 tumors established in C57BL/6NCrl mice (Hu et al., 2020). In neither of these manuscripts was the direct binding of **BMS-202** to the *m*PD-L1 verified before moving to *in vivo* examination. In our hands, such interaction is not allowed, which somehow suggests the involvement of some off-target rather than PD-L1-dependent effects of the *in vivo* therapy presented in these studies.

In other studies, two peptide-based PD-1/PD-L1 inhibitors were tested in syngeneic mouse models (Liu et al., 2019; Sasikumar et al., 2019). In these studies, however, *in vivo* experiments were preceded by either the *in vitro* examination of *m*PD-1/*m*PD-L1 blockade (Liu et al., 2019) or the proliferation rescue and IFN-γ release assay on mouse splenocytes inhibited with the *m*PD-L1 protein (Sasikumar et al., 2019). Still, the direct binding of the tested agents to the *m*PD-L1 protein was not confirmed. Our data provided in this manuscript suggest that extreme caution is required when choosing fully mouse setups for *in vivo* evaluation of anti-cancer properties of PD-L1-targeting agents. This is because some of these agents clearly provide only human-specific therapeutic activities. Therefore, proper controls leaving no doubts as for successful targeting of the mouse PD-L1 are essential before attributing the observed biological effects to the PD-1/PD-L1 checkpoint blockade.

By now, several setups of the humanized mouse systems for immuno-oncology have been proposed (De La Rochere et al., 2018). This includes immunocompetent knock-in mice expressing either fully human or human/mouse hybrids of the proteins of interest, and immunodeficient mice that support the recapitulation of the human immune system and the engraftment of human cell lines and patient-derived xenografts (PDX). These systems are believed to provide optimal platforms for the evaluation of human PD-L1-specific drug candidates. In addition, some other setups have also been proposed, such as the implantation of the mixture of pre-activated PBMCs and human H460-Luc cells into the flank of BALB/c nude mice followed by the treatment with anti-PD-L1 peptide (Li et al., 2018). Such a setup provides a trial for eliminating the need for validating the mouse PD-L1-specificity of the experimental treatment. Still, it is not devoid of possible effects that may alter the interpretation of the results.

In conclusion, this manuscript proves for the structural similarity of the human and mouse PD-L1 protein but points out important differences in the druggability of these two proteins. It is also a guide for the followers, that a proper *in vitro* analysis done on either the isolated mouse protein or using a 'murinized' cell-based assay presented in this work is obligatory before starting *in vivo* studies, and that *in silico* analysis may be simply insufficient to provide reliable predictions of species specificity of the used molecule.

Limitations of the study

In the present study, we present the first structure of the PD-1-interacting domain of a mouse PD-L1 protein. It is worth mentioning that for human PD-L1 crystal structures of the whole, two-domain extracellular part of the protein, are available (see Figure 1). As for today, the two-domain structure of the mouse PD-L1 remains unsolved. We also present that mouse PD-L1 is able to interact with the human PD-1 protein and bring an inhibitory signal toward the activated Jurkat T cells *in vitro*. Whether the functional immune checkpoint would be provided by the interaction of *m*PD-L1 with *h*PD-1 *in vivo* remains unknown.

Resource availability

Lead contact

Further information and requests for resources and reagents should be directed to and will be fulfilled by the lead contact, Lukasz Skalniak (lukasz.skalniak@uj.edu.pl).

Materials availability

The plasmids and cell lines generated in this study will be made available on request, but we may require payment covering of the shipment fee, and/or a completed Materials Transfer Agreement if there is potential for commercial application.

Data and code availability

The accession number for the N-terminal PD-1-binding domain of the *m*PD-L1 protein (amino acids 19-134) reported in this paper is PDB: 6SRU.

Methods

All methods can be found in the accompanying Transparent methods supplemental file.

Supplemental information

Supplemental Information can be found online at https://doi.org/10.1016/j.isci.2020.101960.

Acknowledgments

This research has been supported by project POIR.04.04.00-00-420F/17-00 which is carried out within the TEAM program of the Foundation for Polish Science co-financed by the European Union under the European Regional Development Fund (to T.A.H.), by the Sonata Grant No. UMO-2018/31/D/NZ7/01900 from the National Science Centre, Poland (to K. M.-M.), and by the Preludium Grant No. UMO- 2019/35/N/NZ5/04435 from the National Science Centre, Poland (to J.K.). K. M.-M. is a recipient of the START fellowship from the Foundation for Polish Science (FNP). J.K. acknowledges the fellowship with project No. POWR.03.02.00-00-I013/16 from the National Center for Research and Development. We acknowledge the MCB Structural Biology Core Facility (supported by the TEAM TECH CORE FACILITY/2017-4/6 grant from the Foundation for Polish Science) for valuable support. The research leading to this result has

been supported by the project CALIPSOplus under the Grant Agreement 730872 from the EU Framework Program for Research and Innovation Horizon 2020. The access to ESRF was financed by the Polish Ministry of Science and High Education - decision number: DIR/WK/2016/19.

Author contributions

Conceptualization, K.M.-M., T.A.H., and L.S.; Methodology, K.M.-M., M.C., and L.S.; Investigation, K.M.-M., J.K., B.M., J.P., D.S., M.M., P.G., M.H., and L.S.; Visualization, K.M.-M., B.M., J.P., and L.S.; Writing – Original Draft, K.M.-M., B.M., J.P., D.S., and L.S.; Writing – Review & Editing, K.M.-M., T.A.H., M.S., and L.S.; Funding Acquisition, K.M.-M., and T.A.H.; Supervision, K.M.-M., T.A.H., M.S., and L.S. First authorship: K.M.-M. was responsible for conceptualization, supervision, and/or performing of the protein-based experiments, while J.K. was responsible for designing and performing cell-based experiments. Corresponding authorship: K.M.-M. was a primary investigator involved in supervision, performing, and describing protein-based experiments, while L.S. was a primary investigator responsible for conceptualization and supervision over cell-based and *in vivo* studies, and for the analysis of the resulting data.

Declaration of interests

The authors declare no competing interests.

Received: July 1, 2020
Revised: October 13, 2020
Accepted: December 15, 2020
Published: January 22, 2021

References

Azuma, T., Yao, S., Zhu, G., Flies, A.S., Flies, S.J., and Chen, L. (2008). B7-H1 is a ubiquitous antiapoptotic receptor on cancer cells. Blood *111*, 3635–3643.

Chae, Y.K., Arya, A., Iams, W., Cruz, M.R., Chandra, S., Choi, J., and Giles, F. (2018). Current landscape and future of dual anti-CTLA4 and PD-1/PD-L1 blockade immunotherapy in cancer; lessons learned from clinical trials with melanoma and non-small cell lung cancer (NSCLC). J. Immunother. Cancer *6*, 39.

Chen, Y., Liu, P., Gao, F., Cheng, H., Qi, J., and Gao, G.F. (2010). A dimeric structure of PD-L1: functional units or evolutionary relics? Protein Cell *1*, 153–160.

Cheng, X., Veverka, V., Radhakrishnan, A., Waters, L.C., Muskett, F.W., Morgan, S.H., Huo, J., Yu, C., Evans, E.J., Leslie, A.J., et al. (2013). Structure and interactions of the human programmed cell death 1 receptor. J. Biol. Chem. *288*, 11771–11785.

De La Rochere, P., Guil-Luna, S., Decaudin, D., Azar, G., Sidhu, S.S., and Piaggio, E. (2018). Humanized mice for the study of immuno-oncology. Trends Immunol. *39*, 748–763.

Francisco, L.M., Salinas, V.H., Brown, K.E., Vanguri, V.K., Freeman, G.J., Kuchroo, V.K., and Sharpe, A.H. (2009). PD-L1 regulates the development, maintenance, and function of induced regulatory T cells. J. Exp. Med. *206*, 3015–3029.

Friedl, P., and Wolf, K. (2003). Tumour-cell invasion and migration: diversity and escape mechanisms. Nat. Rev. Cancer *3*, 362–374.

Guzik, K., Tomala, M., Muszak, D., Konieczny, M., Hec, A., Błaszkiewicz, U., Pustuła, M., Butera, R., Dömling, A., and Holak, T.A. (2019). Development of the inhibitors that target the PD-1/PD-L1 interaction-A brief look at progress on small molecules, peptides and macrocycles. Molecules *24*, 1–30.

Guzik, K., Zak, K.M., Grudnik, P., Magiera, K., Musielak, B., Törner, R., Skalniak, L., Dömling, A., Dubin, G., and Holak, T.A. (2017). Small-molecule inhibitors of the programmed cell death-1/programmed death-ligand 1 (PD-1/PD-L1) interaction via transiently induced protein states and dimerization of PD-L1. J. Med. Chem. *60*, 5857–5867.

Hansel, T.T., Kropshofer, H., Singer, T., Mitchell, J.A., and George, A.J.T. (2010). The safety and side effects of monoclonal antibodies. Nat. Rev. Drug Discov. *9*, 325–338.

Herbst, R.S., Soria, J.-C., Kowanetz, M., Fine, G.D., Hamid, O., Gordon, M.S., Sosman, J.A., McDermott, D.F., Powderly, J.D., Gettinger, S.N., et al. (2014). Predictive correlates of response to the anti-PD-L1 antibody MPDL3280A in cancer patients. Nature *515*, 563–567.

Hoos, A. (2016). Development of immuno-oncology drugs - from CTLA4 to PD1 to the next generations. Nat. Rev. Drug Discov. *15*, 235–247.

Hu, Z., Yu, P., Du, G., Wang, W., Zhu, H., Li, N., Zhao, H., Dong, Z., Ye, L., and Tian, J. (2020). PCC0208025 (BMS202), a small molecule inhibitor of PD-L1, produces an antitumor effect in B16-F10 melanoma-bearing mice. PLoS One *15*, e0228339.

Krajewski, M., Rothweiler, U., D'Silva, L., Majumdar, S., Klein, C., and Holak, T.A. (2007). An NMR-based antagonist induced dissociation assay for targeting the ligand-protein and protein-protein interactions in competition binding experiments. J. Med. Chem. *50*, 4382–4387.

Larkin, J., Chiarion-Sileni, V., Gonzalez, R., Grob, J.-J., Rutkowski, P., Lao, C.D., Cowey, C.L., Schadendorf, D., Wagstaff, J., Dummer, R., et al. (2019). Five-year survival with combined nivolumab and ipilimumab in advanced melanoma. N. Engl. J. Med. *381*, 1535–1546.

Lázár-Molnár, E., Yan, Q., Cao, E., Ramagopal, U., Nathenson, S.G., and Almo, S.C. (2008). Crystal structure of the complex between programmed death-1 (PD-1) and its ligand PD-L2. Proc. Natl. Acad. Sci. U S A *105*, 10483–10488.

Lee, H.T., Lee, J.Y., Lim, H., Lee, S.H., Moon, Y.J., Pyo, H.J., Ryu, S.E., Shin, W., and Heo, Y.-S. (2017). Molecular mechanism of PD-1/PD-L1 blockade via anti-PD-L1 antibodies atezolizumab and durvalumab. Sci. Rep. *7*, 5532.

Lee, H.T., Lee, S.H., and Heo, Y.-S. (2019). Molecular interactions of antibody drugs targeting PD-1, PD-L1, and CTLA-4 in immuno-oncology. Molecules *24*, 1190.

Li, C., Zhang, N., Zhou, J., Ding, C., Jin, Y., Cui, X., Pu, K., and Zhu, Y. (2018). Peptide blocking of PD-1/PD-L1 interaction for cancer immunotherapy. Cancer Immunol. Res. *6*, 178–188.

Lin, D.Y.-W., Tanaka, Y., Iwasaki, M., Gittis, A.G., Su, H.-P., Mikami, B., Okazaki, T., Honjo, T., Minato, N., and Garboczi, D.N. (2008). The PD-1/PD-L1 complex resembles the antigen-binding Fv domains of antibodies and T cell receptors. Proc. Natl. Acad. Sci. U S A *105*, 3011–3016.

Liu, H., Zhao, Z., Zhang, L., Li, Y., Jain, A., Barve, A., Jin, W., Liu, Y., Fetse, J., and Cheng, K. (2019). Discovery of low-molecular weight anti-PD-L1

peptides for cancer immunotherapy. J. Immunother. Cancer *7*, 270.

Magiera-Mularz, K., Skalniak, L., Zak, K.M., Musielak, B., Rudzinska-Szostak, E., Berlicki, Ł., Kocik, J., Grudnik, P., Sala, D., Zarganes-Tzitzikas, T., et al. (2017). Bioactive macrocyclic inhibitors of the PD-1/PD-L1 immune checkpoint. Angew. Chem. Int. Ed. *56*, 13732–13735.

Magnez, R., Thiroux, B., Taront, S., Segaoula, Z., Quesnel, B., and Thuru, X. (2017). PD-1/PD-L1 binding studies using microscale thermophoresis. Sci. Rep. *7*, 17623.

Sasikumar, P.G., Ramachandra, R.K., Adurthi, S., Dhudashia, A.A., Vadlamani, S., Vemula, K., Vunnum, S., Satyam, L.K., Samiulla, D.S., Subbarao, K., et al. (2019). A rationally designed peptide antagonist of the PD-1 signaling pathway as an immunomodulatory agent for cancer therapy. Mol. Cancer Ther. *5407*, molcanther.0737.2018.

Shaabani, S., Huizinga, H.P.S.S., Butera, R., Kouchi, A., Guzik, K., Magiera-Mularz, K., Holak, T.A., and Dömling, A. (2018). A patent review on PD-1/PD-L1 antagonists: small molecules, peptides, and macrocycles (2015-2018). Expert Opin. Ther. Pat. *28*, 665–678.

Skalniak, L., Zak, K.M., Guzik, K., Magiera, K., Musielak, B., Pachota, M., Szelazek, B., Kocik, J., Grudnik, P., Tomala, M., et al. (2017). Small-molecule inhibitors of PD-1/PD-L1 immune checkpoint alleviate the PD-L1-induced exhaustion of T-cells. Oncotarget *8*, 72167–72181.

Tang, S., and Kim, P.S. (2019). A high-affinity human PD-1/PD-L2 complex informs avenues for small-molecule immune checkpoint drug discovery. Proc. Natl. Acad. Sci. U S A *116*, 24500–24506.

Topalian, S.L., Drake, C.G., and Pardoll, D.M. (2015). Immune checkpoint blockade: a common denominator approach to cancer therapy. Cancer Cell *27*, 450–461.

Yang, J., and Hu, L. (2019). Immunomodulators targeting the PD-1/PD-L1 protein-protein interaction: from antibodies to small molecules. Med. Res. Rev. *39*, 265–301.

Zak, K.M., Kitel, R., Przetocka, S., Golik, P., Guzik, K., Musielak, B., Dömling, A., Dubin, G., and Holak, T.A. (2015). Structure of the complex of human programmed death 1, PD-1, and its ligand PD-L1. Structure *23*, 2341–2348.

Zak, K.M., Grudnik, P., Guzik, K., Zieba, B.J., Musielak, B., Dömling, A., Dubin, G., and Holak, T.A. (2016). Structural basis for small molecule targeting of the programmed death ligand 1 (PD-L1). Oncotarget *7*, 30323–30335.

Zak, K.M., Grudnik, P., Magiera, K., Dömling, A., Dubin, G., and Holak, T.A. (2017). Structural Biology of the immune checkpoint receptor PD-1 and its ligands PD-L1/PD-L2. Structure *25*, 1163–1174.

Zhang, X., Schwartz, J.-C.D., Guo, X., Bhatia, S., Cao, E., Lorenz, M., Cammer, M., Chen, L., Zhang, Z.-Y., Edidin, M.A., et al. (2004). Structural and functional analysis of the costimulatory receptor programmed death-1. Immunity *20*, 337–347.

Zhang, L., Gajewski, T.F., and Kline, J. (2009). PD-1/PD-L1 interactions inhibit antitumor immune responses in a murine acute myeloid leukemia model. Blood *114*, 1545–1552.

Zhang, F., Wei, H., Wang, X., Bai, Y., Wang, P., Wu, J., Jiang, X., Wang, Y., Cai, H., Xu, T., and Zhou, A. (2017). Structural basis of a novel PD-L1 nanobody for immune checkpoint blockade. Cell Discov. *3*, 17004.

Zhang, R., Zhu, Z., Lv, H., Li, F., Sun, S., Li, J., and Lee, C.-S. (2019). Immune checkpoint blockade mediated by a small-molecule nanoinhibitor targeting the PD-1/PD-L1 pathway synergizes with photodynamic therapy to elicit antitumor immunity and antimetastatic effects on breast cancer. Small *1903881*, e1903881.

Zitvogel, L., Tesniere, A., and Kroemer, G. (2006). Cancer despite immunosurveillance: immunoselection and immunosubversion. Nat. Rev. Immunol. *6*, 715–727.

Zitvogel, L., Pitt, J.M., Daillère, R., Smyth, M.J., and Kroemer, G. (2016). Mouse models in oncoimmunology. Nat. Rev. Cancer *16*, 759–773.

iScience, Volume *24*

Supplemental Information

Human and mouse PD-L1: similar molecular structure, but different druggability profiles

Katarzyna Magiera-Mularz, Justyna Kocik, Bogdan Musielak, Jacek Plewka, Dominik Sala, Monika Machula, Przemyslaw Grudnik, Malgorzata Hajduk, Marcin Czepiel, Maciej Siedlar, Tad A. Holak, and Lukasz Skalniak

Supplemental data items

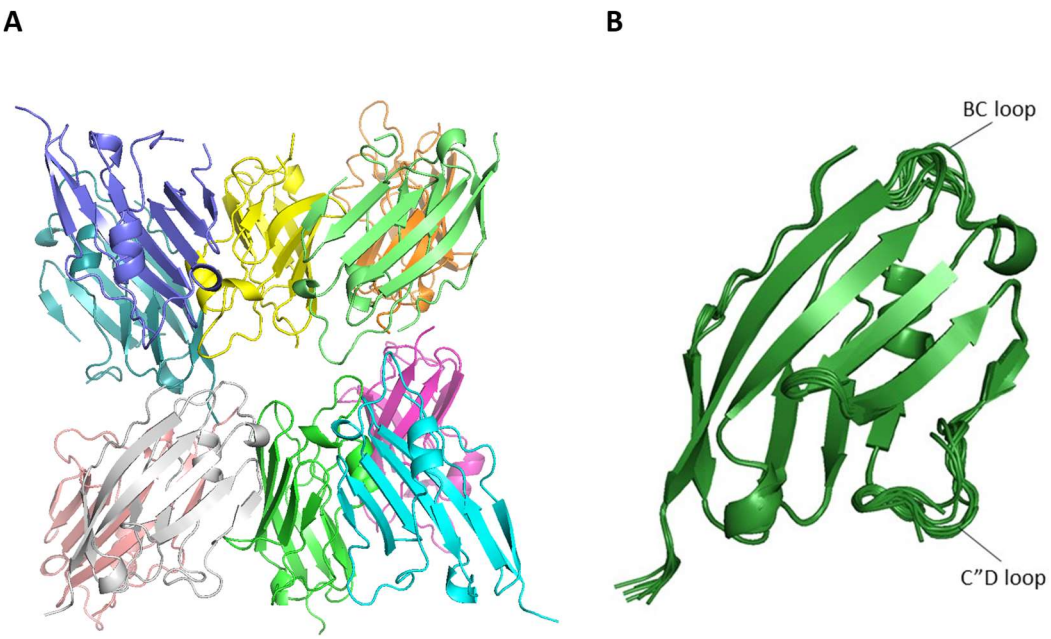

Figure S1. The overall structure of mouse apo-PD-L1. Related to Figure 2. A. The asymmetric unit is composed of 10 chains of *m*PD-L1. B. Superposition of the *m*PD-L1 chains from the ten copies. The most variable regions (BC and C"D loops) are shown.

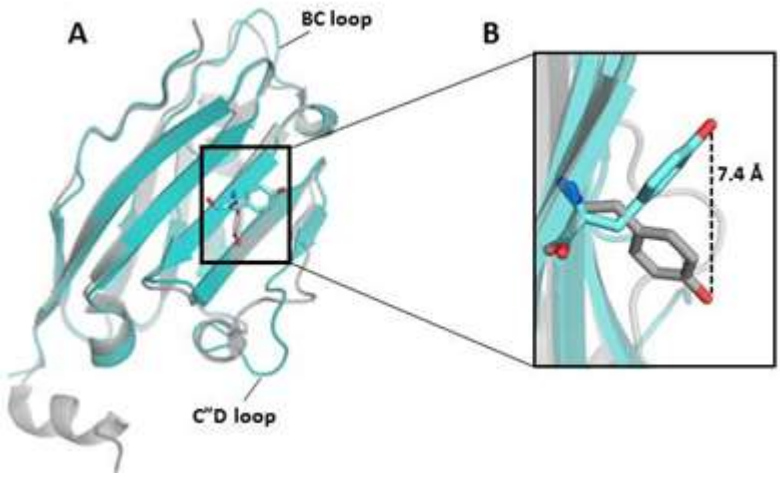

Figure S2. The rearrangement of Tyr56 sidechain between the human and mouse PD-L1 proteins. Related to Figure 2. A. The superposition of PD-1-binding domains of the human (grey, PDB: 5C3T) and mouse (cyan, PDB: 6SRU) PD-L1 proteins. B**.** Close-up view of the rearrangement of Tyr56 sidechain in the *m*PD-L1 structure compared to the *h*PD-L1 structure.

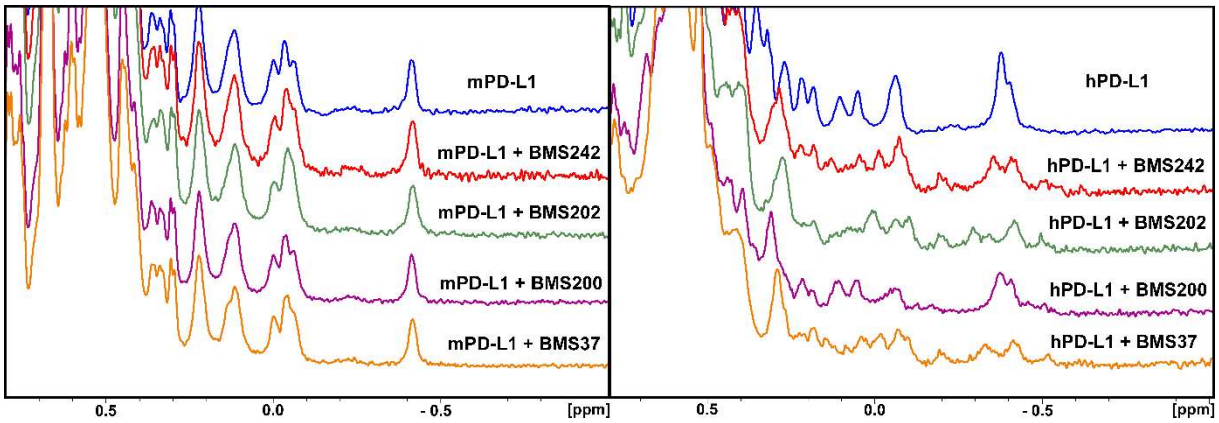

Figure S3. The aliphatic region ^{1}H NMR spectra of PD-L1 proteins. Related to Figure 4. Left panel: ^{1}H NMR spectra of apo-*m*PD-L1 (blue) and titrated *m*PD-L1 with BMS-242 (red), BMS-202 (green), BMS-200 (purple), BMS-37 (orange) at 2:1 molar ratio. Right panel: ^{1}H NMR spectra of apo-*h*PD-L1 (blue) and *h*PD-L1 with BMS-242 (red), BMS-202 (green), BMS-200 (purple), BMS-37 (orange) at 1:2 molar ratio. Linewidth broadening of the NMR signals and changes in the aliphatic region are only visible in *h*PD-L1 spectra that suggests no interaction between *m*PD-L1 and BMS compounds.

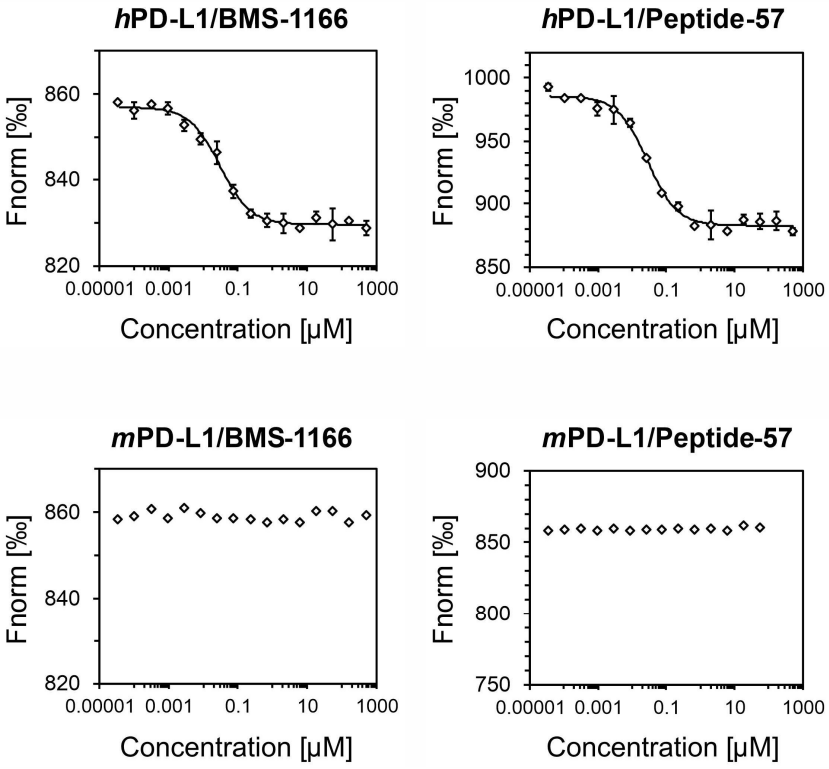

Figure S4. The interaction of BMS-1166 and peptide-57 with either *h*PD-L1 (upper panels), or *m*PD-L1 (lower panels) was tested with MicroScale Thermophoresis (MST) binding assay. Related to Figure 4.

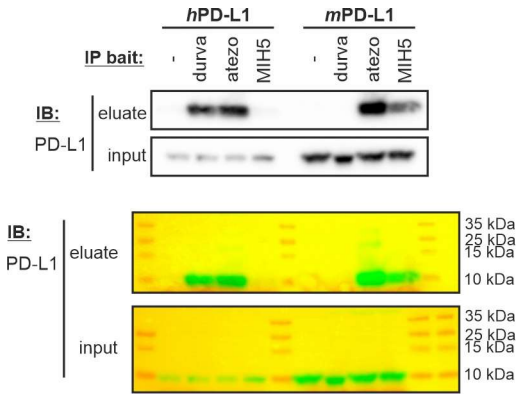

Figure S5. Co-immunoprecipitation of *h*PD-L1 and *m*PD-L1 with the use of diverse monoclonal antibodies. Related to Figure 5. Co-immunoprecipitation assay performed with the use of beads coated with the indicated anti-PD-L1 antibodies (bait), incubated with either *h*PD-L1, or *m*PD-L1 (prey). The figure shows data representative for three independent experiments. The bottom panel presents immunoblot results (green) superimposed with a bright-field image of the membrane with visible protein standards (PageRuler™ Prestained Protein Ladder, red). Molecular weights of the proteins corresponding to protein ladder bands are provided on the right side of the images.

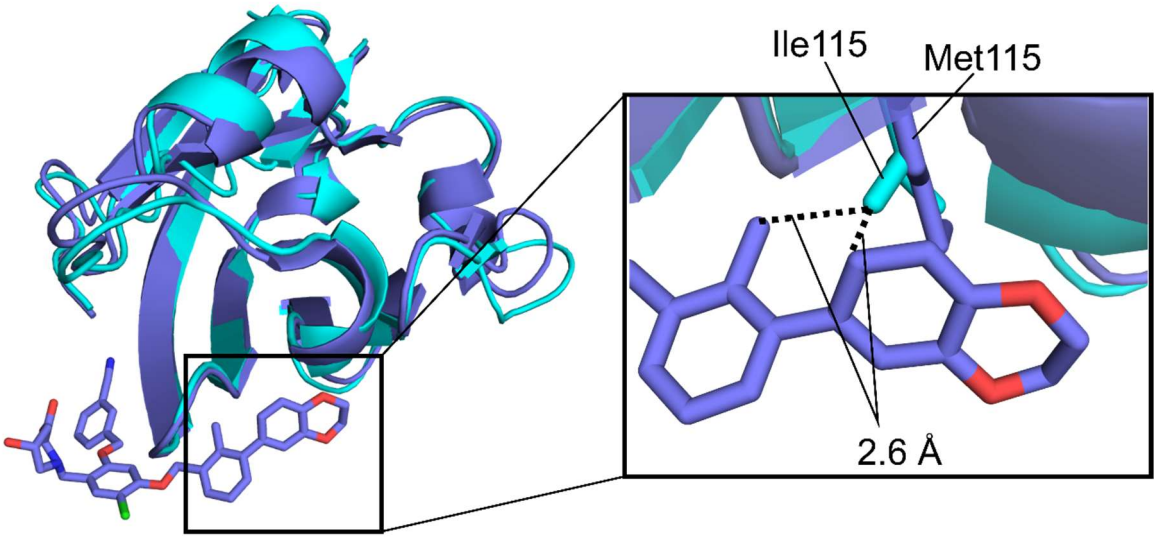

Figure S6. Overlap of *h*PD-L1/BMS-1001 (blue; PDB: 6R3K) and *m*PD-L1 (cyan; PDB: 6SRU) structures. Related to Figure 6. Ile115 (in mouse structure) can sterically collide with biphenyl moiety of BMS-compounds.

Table S1. The list of amino acids involved in the interactions between human PD-L1 (*h*PD-L1) and antibodies, small molecule BMS-1166, and peptide-57, along with the list of corresponding amino acids in the sequence of mouse PD-L1 (*m*PD-L1). Related to Figure 6. Different amino acids in mouse sequence are highlighted in bold. Adapted from Lee et al. (Lee et al., 2017)

Atezolizumab		**Durvalumab**	
*h*PD-L1 contact residues	analogous *m*PD-L1 residues	*h*PD-L1 contact residues	analogous *m*PD-L1 residues
A18	A18	T20	T20
E45	E45	V23	**A23**
D49	D49	D26	D26
A51	**L51**	Y56	Y56
A52	A52	E58	E58
I54	**V54**	E60	E60
Y56	Y56	D61	D61
E58	E58	V111	V111
E60	E60	R113	**C113**
D61	D61	M115	**I115**
N63	**Q63**	A121	A121
Q66	Q66	D122	D122
V68	V68	Y123	Y123
H69	**A69**	K124	K124
V111	V111	R125	R125
R113	**C113**	T127	T127
M115	**I115**		
S117	S117		
Y118	Y118		
G119	G119		
A121	A121		
Y123	Y123		
R125	R125		

peptide-57		**BMS-1166 $_{A}$PD-L1 subunit, see** (Skalniak et al., 2017)	
*h*PD-L1 contact residues	analogous *m*PD-L1 residues	*h*PD-L1 contact residues	analogous *m*PD-L1 residues
I54	**V54**	I54	**V54**
Y56	Y56	Y56	Y56
E58	E58	M115	**I115**
N63	**Q63**	A121	A121
Q66	Q66	D122	D122
V68	V68	Y123	Y123
R113	**C113**	K124	K124
M115	**I115**	R125	R125
A121	A121		
Y123	Y123		

Transparent methods

Materials

In the study, the following antibodies were used: anti-PD-1 therapeutic antibodies nivolumab (Opdivo, Bristol-Myers Squibb) and pembrolizumab (Keytruda, Merck), anti-PD-L1 therapeutic antibodies atezolizumab (Selleck Chemicals, cat. A2004) and durvalumab (Selleck Chemicals, cat. A2013), anti-human PD-L1 antibody clone MIH1 (eBioscience, cat. 14-5983-82), anti-mouse PD-L1 antibody clone MIH5 (eBioscience, cat. 14-5982-82), anti-mouse PD-L1- Purified *in vivo* PLATINUM™ Functional Grade clone 10F.9G2 (Leinco Technologies, Inc., cat. P371). The following small molecular PD-1/PD-L1-blockers developed by Bristol-Myers Squibb were used: BMS-37, BMS-200, BMS-202, BMS-242, BMS-1001, and BMS-1166, prepared as described before (Guzik et al., 2017). The macrocyclic peptide-57 was obtained from Pepmic Co., Ltd.

Protein Expression and Purification

The IgV domains of human and mouse PD-L1 protein (*h*PD-L1 residues: 18-134, C-terminal His-tag; *m*PD-L1 residues: 19-134) and the extracellular domain of human PD-1 (*h*PD-1 residues 34-150, C93S) were expressed and purified as described previously (Zak et al., 2016). Briefly, proteins were expressed in *E*. coli BL21 (DE3) strain as inclusion bodies which were collected by centrifugation, washed, and dissolved using the 6M GuHCl buffer. Proteins were refolded by drop-wise dilution into refolding buffers: 0.1 M Tris pH 8.0, 1 M L-Arg hydrochloride, 2 mM EDTA, 0.25 mM oxidized glutathione and 0.25 mM reduced glutathione for both PD-L1 proteins and 0.1 M Tris pH 8.0, 0.4 M L-Arg hydrochloride, 2 mM EDTA, 5 mM cystamine and 0.5 mM cysteamine for the *h*PD-1 protein. Refolded proteins were dialyzed 3 times over 48-72 h against buffer containing 10 mM Tris pH 8.0 and 20 mM NaCl. On the final step, proteins were concentrated and loaded to a size exclusion chromatography column HiLoad 26/600 Superdex 75 (GE Healthcare) pre-equilibrated with buffer containing 10 mM Tris pH 8.0 and 20 mM NaCl.

Crystallization of apo-mPD-L1

Purified *m*PD-L1 was concentrated to 5 mg/ml and the crystallization screening was carried out using commercially available buffer sets. Initially obtained crystals were optimized. Diffraction-quality crystals were obtained at room temperature from the condition containing: 0.2 M ammonium sulfate, 0.1 M Tris pH 7.5, 20% PEG 5000 MME. The crystal was flash-cooled in liquid nitrogen without cryoprotection.

Crystal structure determination and refinement

The X-ray diffraction data were collected at the beamline ID23-1 at the ESRF (Grenoble, France) (Nurizzo et al., 2006). The data were indexed, integrated, and scaled using XDS, XSCALE, and Aimless (Evans and Murshudov, 2013; Kabsch, 2010; Krug et al., 2012). Initial phases were obtained by molecular replacement calculated in Phaser (McCoy et al., 2007). The model building was performed in Coot and refinement was performed using Phenix or PDB-REDO server (Adams et al., 2010; Emsley and Cowtan, 2004; Joosten et al., 2014). Water molecules were added automatically and inspected manually. Coordinates and structure factors were deposited in the Protein Data Bank under accession code PDB: 6SRU.

NMR Experiments

Uniform ^{15}N labeling was obtained by expressing the proteins in the M9 minimal medium containing $^{15}NH_4Cl$ as a source of nitrogen. For NMR measurements, the buffer was exchanged to PBS pH 7.4 or 25 mM sodium phosphate pH 6.4 containing 100 mM NaCl for PD-L1 proteins or the *h*PD-1 protein, respectively. 10% (v/v) of D_2O was added to the samples to provide the lock signal. All spectra were recorded at 300 K using a Bruker Avance 600 MHz spectrometer equipped with cryo-probehead.

MST binding assay

*h*PD-1 was labeled with RED-NHS 2nd Generation dye from NanoTemper according to the attached protocol and diluted to final the concentration of 20 nM. *h*PD-1 was titrated with either *m*PD-L1 at the final concentrations from 0.0174 to 570 µM or *h*PD-L1 at the final concentration from 0.416 to 183 µM in PBS buffer with 0.005% Tween-20 and left for 1h incubation at room temperature. The MST

measurement was performed on Monolith NT.115 series using high precision capillaries at Excitation Power and MST Power of 40% in triplicates. The results were fitted with Hill's model using MO. Affinity Analysis v2.3 with a cold region at -1 s and hot region from 0.5 to 1.5 s for mPD-L1 and 4 to 5 s for *h*PD-L1.

Cell lines

Mouse skin melanoma B16-F10 cell line was obtained from the American Type Culture Collection (ATCC). Chinese hamster ovary CHO-K1 cell line was purchased from the European Collection of Authenticated Cell Cultures (ECACC). Artificial antigen-presenting (aAPCs) CHO-K1 cells expressing TCR Activator, CHO-K1 cells expressing TCR Activator, and overexpressing PD-L1 (aAPCs/PD-L1), as well as Jurkat T Effector Cells (ECs) overexpressing PD-1 and containing the Luciferase gene controlled by NFAT Response Element (NFAT-RE) were acquired from Promega. All cell lines were cultured in RPMI-1640 (Biowest) supplemented with 10% Fetal Bovine Serum (FBS, Biowest) and 200 mM L-Glutamine (Biowest). To sustain the stable transfection, aAPCs were cultured in the presence of Hygromycin B Gold (50 µg/ml, InvivoGen), while aAPCs/PD-L1 and ECs were cultured in the presence of Hygromycin B Gold (50 µg/ml, InvivoGen) and G418 (250 µg/ml, InvivoGen). The overexpression of PD-1 and PD-L1 was confirmed by flow cytometry, while the expression of TCR Activator was confirmed by western blotting. MC38 cells (Kerafast) were cultured in DMEM containing 4.5 g/l of glucose, and supplemented with 10% FBS and 200 mM L-Glutamine. The cells were routinely controlled for *Mycoplasma sp.* contamination with the PCR-based method (van Kuppeveld et al., 1992).

*The preparation of the B16-F10/TCRAct cells (*m*aAPCs)*

For the generation of the B16-F10/TCRAct cells (*m*aAPCs), B16-F10 cells were transfected with the pcDNA3.1 (+) plasmid (Invitrogen) encoding TCRAct hybrid protein, composed of the human CD5 membrane-localization sequence, scFv fragment of the OKT3 antibody, and the transmembrane fragment of the human CD28 (CD5-scFv OKT3-CD28) (Leitner et al., 2010). The transfection was done using Lipofectamine 2000 (Invitrogen). Stable transfectants were selected with 1 mg/ml of G418. The expression of TCRAct was verified first by the functional assay (the *h*/*m*ICB assay, see below) and by the western blot with the use of anti-CD28 antibody clone EPR22076. For the experiments, the clone named 3C4 was used.

Flow cytometry

For the flow cytometry analysis the cells were detached from the plates with TrypLE Select Enzyme (Gibco), placed on ice, washed two times with Flow Cytometry Staining Buffer (eBioscience) and stained with primary fluorophore-conjugated antibodies: PE-conjugated rat anti-mouse PD-L1 antibody clone MIH5 (eBioscience, cat. 12-5982-82), PE-conjugated rat IgG2a kappa isotype control clone eBR2a (eBioscience, cat. 12-4321-80), APC-conjugated mouse anti-human PD-L1 antibody clone MIH1 (eBioscience, cat. 17-5983-42), APC-conjugated mouse IgG1 kappa isotype control clone P3.6.2.8.1 (eBioscience, cat. 17-4714-82). Samples were analyzed with FACSVerse flow cytometer (Becton Dickinson, BD) and BD FACSuite™ Software.

Western blotting

The cell lysates were prepared with RIPA buffer (Sigma-Aldrich) containing Protease Inhibitor Cocktail (Sigma-Aldrich). The lysates were separated by 12% SDS-PAGE (TGX™ FastCast™ Acrylamide Kit, Bio-Rad) and transferred into a PVDF membrane (Merck Millipore) using a Mini Trans-Blot® Cell system (Bio-Rad) at 100 V for 1.5 h on ice. The membranes were incubated in 4% (m/v) bovine serum albumin (BioShop) in TBS buffer containing 0.1% (v/v) Nonidet P-40 (BioShop) at RT for 1 h. Then, the membranes were incubated with specific primary antibody at 4°C overnight. Following three washes in TBS-N, the secondary horseradish peroxidase (HRP)-conjugated antibody was applied for 1 h at RT. After three additional washes in TBS-N, the visualization of protein with Clarity Western ECL Substrate (Bio-Rad) and ChemiDoc MP Imaging System (Bio-Rad) was carried out according to the manufacturer's instructions.

The proteins of interest were detected with primary antibodies: rabbit monoclonal anti-CD28 antibody at a 1:1,000 dilution (EPR22076, Abcam, cat. ab243228), rabbit monoclonal anti-α-tubulin at 1:2,000 (11H10, Cell Signaling Technology, CST, cat. 2125), and the goat HRP-linked anti-rabbit secondary antibody at 1:3,000 (CST, cat.7074).

Immune Chceckpoint Blockade (ICB) assay

Artificial antigen presenting cells: CHO/TCRAct/PD-L1(aAPCs, used in the *h*/*h*ICB assay) and B16-F10/TCRAct (*m*aAPCs, used in the *h*/*m*ICB assay), as well as the initial CHO K1 and B16-F10 cells were either seeded on 96-well plates at the density of 10,000 cells/well and processed, or seeded at the density of 2,000 cells/well and treated with 20 ng/ml of mouse recombinant IFN-γ (Thermo Fisher Scientific) for 48 hours before processing. The culture medium was discarded and the wells were gently washed two times using fresh portion of culture medium to remove residual IFN-γ. Jurkat T cells overexpressing PD-1 and luciferase gene controlled by the NFAT-response element (Jurkat Effector Cells, Jurkat-ECs) were subsequently added to the aAPCs and *m*aAPCs at the density 20,000 cells/well, and cells were incubated in the assay buffer (99% RPMI 1640, 1% FBS) in the presence of PD-1/PD-L1 inhibitors for 24h. The luminescence was measured after the addition of Bio-Glo™ Assay reagent (Promega), according to the manufacturer's instructions, using the Infinite M200 plate reader (TECAN).

The stock solutions of small-molecules and the peptide-57 were first prepared in DMSO (2 mM and 10 mM stock solutions) and subsequently diluted in the assay buffer at a ratio 1:1,000. Due to the addition of the ECs, the final concentrations of the compounds were 1 µM and 5 µM, as indicated in the figures. The dilutions of the monoclonal antibodies were performed in the assay buffer prior to the experiments, to obtain the final concentrations of 0.25 µg/ml and 1 µg/ml.

Co-immunoprecipitation

For immunoprecipitation 25 µg/ml of antibodies (durvalumab/atezolizumab/MIH5) in PBS with 0,02% (v/v) Tween 20 (Bio-Rad) were incubated for 10 minutes with Dynabeads™ Protein G (Thermo Fisher Scientific, cat. 10004D). Then, Protein G-Abs complexes were incubated with IgV domains of *m*PD-L1 or *h*PD-L1 (see Protein Expression and Purification section) in the same concentrations of 2µg/ml in PBS with 1% (m/v) bovine serum albumin (BioShop) for 15 minutes. Samples were washed three times with 200 µl PBS and suspended in 100 µl of PBS. To get rid of beads coated with Protein G, the samples were denaturated with SDS-PAGE sample buffer and analyzed on WB with PD-L1 (N) Rabbit Polyclonal Primary Antibody at a 1:2,000 dilution (Abiocode, cat. R0586-1) and HRP-Linked Anti-Rabbit Secondary Antibody at a 1:3,000 dilution (CST, cat. 7074).

Syngeneic mouse model

For the *in vivo* study, 6–10-weeks-old C57BL/6 mice (Janvier Labs) were used. Tumor cell line MC38 cells ($5x10^5$ cells) were injected subcutaneously in 50 µl of sterile PBS into a single flank of each experimental mouse. At the day 5 following the injection, three mice that developed measurable tumors were excluded from the experiment. The mice were randomly divided into three groups, each containing 9 animals. Therapeutic antibodies, atezolizumab and durvalumab, as well as control anti-mouse PD-L1 antibody clone 10F.9G2 were injected intraperitonealy at the dose of 200 µg in 200 µl of physiological salt at the days 5, 9, and 13 following the injection. The growth of the tumors was monitored every 2-3 days by measuring two perpendicular diameters of the tumors and calculating tumor size as the tumor surface equal to the product of these diameters (mm^2). The mice were sacrified either when the tumor exceeded the size of 250 mm^2 or at the day 30 of the experiment. The tumor growth data was analyzed using the TumGrowth online tool (Enot et al., 2018) with the following settings: no Automatic outlier detection, no Check group-heteroskedacity. Statistical significance was tested using ANOVA and Holm post-hoc test for pairwise comparisons.

Supplemental References

Adams, P.D., Afonine, P. V, Bunkóczi, G., Chen, V.B., Davis, I.W., Echols, N., Headd, J.J., Hung, L.-W., Kapral, G.J., Grosse-Kunstleve, R.W., McCoy, A.J., Moriarty, N.W., Oeffner, R., Read, R.J., Richardson, D.C., Richardson, J.S., Terwilliger, T.C., Zwart, P.H., 2010. PHENIX: a comprehensive Python-based system for macromolecular structure solution. Acta Crystallogr. D. Biol. Crystallogr. 66, 213–21.

Emsley, P., Cowtan, K., 2004. Coot: model-building tools for molecular graphics. Acta Crystallogr. D. Biol. Crystallogr. 60, 2126–32.

Enot, D.P., Vacchelli, E., Jacquelot, N., Zitvogel, L., Kroemer, G., 2018. TumGrowth: An open-access web tool for the statistical analysis of tumor growth curves. Oncoimmunology 7, e1462431.

Evans, P.R., Murshudov, G.N., 2013. How good are my data and what is the resolution? Acta Crystallogr. D. Biol. Crystallogr. 69, 1204–14.

Joosten, R.P., Long, F., Murshudov, G.N., Perrakis, A., 2014. The PDB_REDO server for macromolecular structure model optimization. IUCrJ 1, 213–20.

Kabsch, W., 2010. XDS. Acta Crystallogr. D. Biol. Crystallogr. 66, 125–32.

Krug, M., Weiss, M.S., Heinemann, U., Mueller, U., 2012. XDSAPP : a graphical user interface for the convenient processing of diffraction data using XDS. J. Appl. Crystallogr. 45, 568–572.

Leitner, J., Kuschei, W., Grabmeier-Pfistershammer, K., Woitek, R., Kriehuber, E., Majdic, O., Zlabinger, G., Pickl, W.F., Steinberger, P., 2010. T cell stimulator cells, an efficient and versatile cellular system to assess the role of costimulatory ligands in the activation of human T cells. J. Immunol. Methods 362, 131–41.

McCoy, A.J., Grosse-Kunstleve, R.W., Adams, P.D., Winn, M.D., Storoni, L.C., Read, R.J., 2007. Phaser crystallographic software. J. Appl. Crystallogr. 40, 658–674.

Nurizzo, D., Mairs, T., Guijarro, M., Rey, V., Meyer, J., Fajardo, P., Chavanne, J., Biasci, J.C., McSweeney, S., Mitchell, E., 2006. The ID23-1 structural biology beamline at the ESRF. J. Synchrotron Radiat. 13, 227–38.

van Kuppeveld, F.J., van der Logt, J.T., Angulo, A.F., van Zoest, M.J., Quint, W.G., Niesters, H.G., Galama, J.M., Melchers, W.J., 1992. Genus- and species-specific identification of mycoplasmas by 16S rRNA amplification. Appl. Environ. Microbiol. 58, 2606–2615.